






RESEARCH ARTICLE | DECEMBER 08 2023

Tuning magnon spectra via interlayer coupling in pseudo-3D nanostructured artificial spin ice arrays

Special Collection: [Magnonics](#)

Julius de Rojas   ; Del Atkinson  ; Adekunle O. Adeyeye  

 Check for updates

Appl. Phys. Lett. 123, 232407 (2023)

<https://doi.org/10.1063/5.0177447>


View
Online


Export
Citation

[CrossMark](#)



Applied Physics Letters

Special Topic:
Advances in Quantum Metrology

Submit Today

 **AIP
Publishing**

 **AIP
Publishing**

Tuning magnon spectra via interlayer coupling in pseudo-3D nanostructured artificial spin ice arrays

Cite as: Appl. Phys. Lett. **123**, 232407 (2023); doi: 10.1063/5.0177447

Submitted: 21 September 2023 · Accepted: 18 November 2023 ·

Published Online: 8 December 2023



View Online



Export Citation



CrossMark

Julius de Rojas,^{1,2,a)}  Del Atkinson,¹  and Adekunle O. Adeyeye^{1,a)} 

AFFILIATIONS

¹Department of Physics, Durham University, Durham DH1 3LE, United Kingdom

²Department of Physics, Oklahoma State University, Stillwater, Oklahoma 74078, USA

Note: This paper is part of the APL Special Collection on Magnonics.

^{a)}Authors to whom correspondence should be addressed: julus.de_rojas@okstate.edu and adekunle.o.adeyeye@durham.ac.uk

ABSTRACT

We have investigated the static and dynamic behavior of “pseudo-3D” trilayer square artificial spin ice structures. The trilayer stack comprises of two ferromagnetic Ni₈₁Fe₁₉ (Permalloy, Py) layers with 30 and 70 nm thickness, separated by a nonmagnetic copper layer of varying thickness from 2 to 40 nm. We show that the copper thickness enables interlayer coupling between layers to be finely controlled, leading to bespoke magnetization states and resonance spectra tuning. Our results demonstrate a further route to control the interaction in artificial spin ices beyond planar structures, enabling tunable magnetization dynamics, a potentially programmable degree of freedom for magnonic and microwave devices.

© 2023 Author(s). All article content, except where otherwise noted, is licensed under a Creative Commons Attribution (CC BY) license (<http://creativecommons.org/licenses/by/4.0/>). <https://doi.org/10.1063/5.0177447>

As electronic device structures approach dimensions ≤ 10 nm, efficiency gains have plateaued due to manufacturing limitations and power supply and cooling restraints,^{1,2} leading to a search for energy efficient, next-generation computing hardware. Magnonics,³ an emerging branch of spintronics, potentially offers low-power transmission and processing of data^{4–9} and has been recognized as a promising candidate for neuromorphic,^{10–14} reservoir,^{15,16} and Boolean computing.^{17–19} The magnetic structure, the “magnonic crystal,” through which the magnons propagate is key to controlling spin-wave behavior. Patterned arrays of nanomagnets (NMs) have recently shown potential applications in bit-patterned media,²⁰ logic devices,^{21,22} and microwave filters,^{23–25} while artificial spin ice (ASI) arrays are attracting considerable attention as functional magnonic crystals.^{26–29} ASI arrays are magnetic metamaterials composed of two-dimensional (2D) planar arrays of NMs that depend on the lattice spacing and the geometrical arrangement between individual NMs to tune the long-range magnetostatic interactions, enabling some control over the collective magnetization states and the resulting spin-wave behavior.

ASI structures have been widely studied, among them square spin ice,³⁰ kagome spin ice,³¹ shakti lattices,³² and tetris lattices,³³ demonstrating complex collective behavior.^{9,34–43} Beyond simple arrays,

locally broken symmetries in closely spaced arrays have been shown to have rich spin-wave spectra.^{15,44,45} Separately, recent research has been directed toward the fabrication of three-dimensional (3D) structures such as scaffolds,⁴⁶ tetrapods,⁴⁷ and nanovolcanoes,⁴⁸ where rich magnetic spin textures not seen in 2D structures appear. Although constructing such complex 3D structures is currently time-consuming, it requires specialized fabrication equipment. However, extending the control and tunability of magnon spectra via control of the third, vertical dimension, using standard lithography techniques, could potentially provide a facile, industry-compatible method of adding an extra dimension for system tunability. Recently, studies have been carried out on the magnetization dynamics of trilayer nanowires⁴⁹ and isolated nanodots⁵⁰ using a nonmagnetic layer to separate two ferromagnetic layers, but the emergent magnetostatic and magnetization dynamics resulting from trilayered NMs in ASI arrays, where more complex magnetization states beyond the classic ASI behavior may appear, has not yet been investigated in ASI-type arrays.

In this work, we investigate the collective static and dynamic magnetization behavior of pseudo-3D square ASI-type arrays, in which each nanomagnet is a trilayer stack composed of two ferromagnetic Ni₈₁Fe₁₉ (Permalloy, Py) layers with thicknesses of 30 and 70 nm, separated by a

nonmagnetic copper layer of varying thickness. We first assessed the distinct static and dynamic behavior of the individual ferromagnetic layers and then examined the effect of varying the thickness of the nonmagnetic spacer layer on the reversal process and ferromagnetic resonance (FMR) mode spectrum. Our results demonstrate that the copper thickness enables interlayer coupling between layers to be finely controlled, leading to bespoke tuning of the magnetization states and ferromagnetic resonance spectra. Micromagnetic simulations confirm interlayer coupling is modified, with the ferromagnetic layers responding differently to the increased thickness. Our results highlight a pathway for tuning the static and dynamic magnetic behavior of ASI arrays for functional applications, offering an important additional degree of freedom.

Figure 1(a) shows a schematic of the finite square ASI arrays studied here, where each NM is a trilayer of Py[70 nm]/Cu[t_{Cu}]/Py [30 nm] with $t_{Cu} = 0$ –40 nm. The ASIs were patterned using deep UV (DUV) photolithography on silicon (100) substrates, as described in Singh and Adeyeye,⁵¹ covering a square area of (4 mm)². Ni₈₁Fe₁₉ and Cu were evaporated using a thermal evaporator with base pressure of 1.1×10^{-7} Torr, deposited at a rate of 0.2 Å/s calibrated using x-ray reflectivity. Deposition was followed by ultrasonic liftoff with acetone and isopropyl alcohol. Scanning electron microscopy (SEM) images shown in Fig. 1(b) confirm good liftoff and uniformity of the NMs over a large area. Each NM has dimensions of 500 nm (l) \times 250 nm (w), spaced edge-to-edge by 650 nm [Fig. 1(b) inset].

Quasi-static magnetization behavior was characterized with a vibrating sample magnetometer (VSM) using the in-plane

configuration to measure magnetization as a function of applied field to generate hysteresis (M–H) loops oriented along $\phi = 0^\circ$ and 45° [Fig. 1(b) inset], with a field range of ± 5 kOe. M is defined as the magnetic moment of each sample and saturation magnetization (M_S) as M at +5 kOe. Figure 1(c) shows the M–H loops at $\phi = 0^\circ$ of the individual Py layers with 30 nm (black) and 70 nm (red) thickness. Alongside the M–H loops are plotted the slope of one-half of the magnetization curves, $(dM/dH)/M_S$ (dotted lines), to highlight the reversal features within the M–H loops, determined by weighted linear least squares regression with a window of five neighboring points. The 30 nm-thick sample shows a clear three-step reversal features, consistent with a combination of near-macrospins and nucleation/annihilation of vortices for nanomagnets aligned with their easy and hard axis with respect to the applied field. In contrast, the M–H loop for the 70 nm-thick Py ASI shows five distinct reversal features, attributed to the nucleation, propagation, and annihilation of two vortices in each nanomagnet. In both cases, the interpretation is supported by the micromagnetic analysis described later.

Dynamic magnetic behavior was measured by ferromagnetic resonance (FMR) spectroscopy using a fixed, in-plane RF field in the range of 8–16 GHz oriented in-plane and orthogonal to an applied external field, H [Fig. 1(a)]. The derivative of the absorbed power with respect to the applied field (dP/dH) was measured as the field was swept from 5 kOe to 0 Oe using a field modulation technique, with a broadband microwave detector diode coupled to a lock-in amplifier. Figure 1(d) shows the corresponding FMR spectra measured at

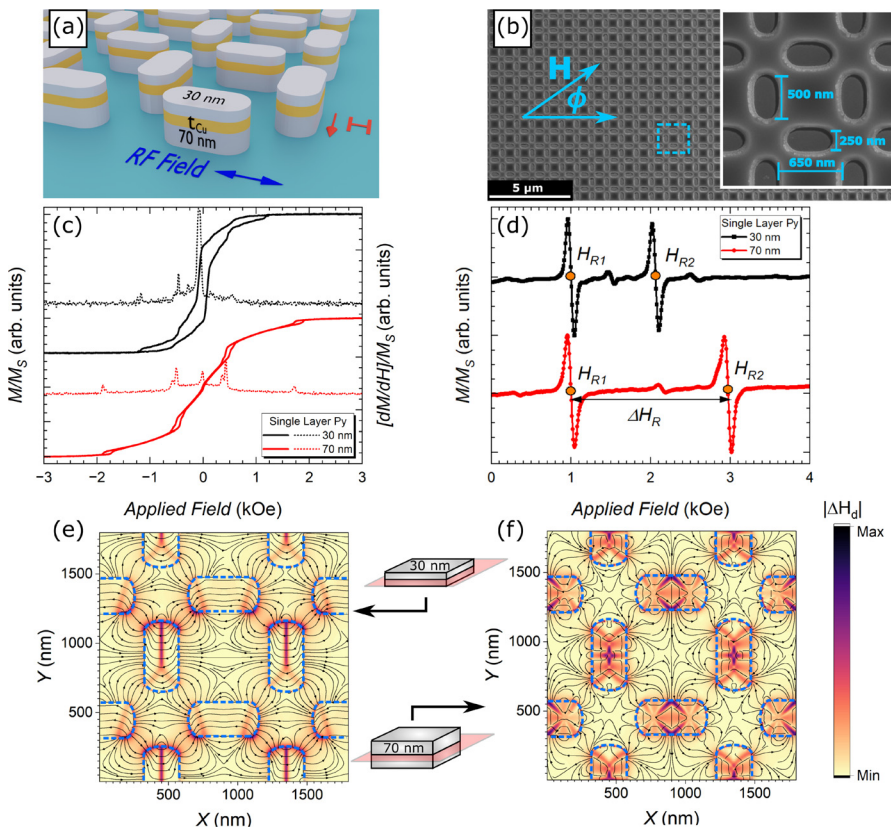


FIG. 1. (a) Schematic of trilayer square ASI array and (b) SEM images of the nanomagnet array. Inset shows magnified image with nanomagnet and array dimensions. (c) and (d) M–H loops (solid lines) alongside $(dM/dH)/M_S$ (dashed lines) and FMR spectra at 12 GHz, respectively, for single layer ASIs of 30 nm-thick (black) and 70 nm-thick (red) Py. The orange dots in (d) indicate resonance fields. (e) and (f) Simulated remanent fields at the midpoint of the 30 and 70 nm-thick Py layers, respectively.

12 GHz for the single 30 nm (black) and 70 nm (red) layers. Two distinct resonance fields are observed during the field sweep along $\phi = 0^\circ$, H_{R1} and H_{R2} . The H_{R1} (H_{R2}) resonance field is associated with ferromagnetic resonances localized in the nanomagnets whose easy (hard) axis is aligned with the applied field. The H_{R1} mode is similar in both layers (near 1.00 kOe), while H_{R2} is higher in the thicker 70 nm layer due to the larger in-plane demagnetization fields.

To understand the effect of increased thickness, micromagnetic simulations of the remanent field within the layers were performed using OOMMF.⁵² The Py parameters used include a saturation magnetization of $M_S = 8.0 \times 10^5$ A/m, a magnetocrystalline anisotropy constant of $K=0$, an exchange constant of $A = 13 \times 10^{-12}$ J/m, a damping parameter of $\alpha = 8.0 \times 10^{-3}$, and a stopping torque of 0.1.⁵³ Array dimensions were obtained from SEM images on a square atlas $(1.8 \mu\text{m})^2$ in area using cubic cells $(5 \text{ nm})^3$ in volume and using 2D periodic boundary conditions.⁵⁴ Figures 1(e) and 1(f) show a vector field plot of the remanent field, H_{db} in the x-y plane at the midpoint of each layer. For the 30 nm thick Py, the NMs whose easy axes are aligned along the applied field have a near macrospin state, while those whose hard axis is along the applied field are near vortex nucleation. In contrast, the remanent fields in the 70 nm layer are in closed-loop states, consistent with a pair vortices of opposite chirality in easy-axis NMs and a single vortex in the hard-axis NMs. For simulated M-H loops and magnetization states at remanence, refer to the supplementary material.

Effectively combining these two single layers, a series of pseudo-3D trilayer nanomagnets in square ASI arrays were synthesized.

Figures 2(a)–2(c) show the M–H loops for trilayer arrays where $t_{Cu} = 2, 20,$ and 40 nm, respectively. We first note the spread of the vortex nucleation/annihilation fields varies significantly across samples. Beginning with the wide spread for $t_{Cu} = 2$ nm [see Fig. 2(a)], we see the spread of nucleation/annihilation fields shrink in width for $t_{Cu} = 20$ nm, centered around 1 kOe [Fig. 2(b)], before shrinking in width further and moving below 1 kOe for $t_{Cu} = 40$ nm [Fig. 2(c)], approaching the features of the 70 nm-thick single layer ASI. Indeed, this is further corroborated by the appearance of reversal features for $\phi = 0^\circ$ near ± 2.1 kOe for the $t_{Cu} = 40$ nm sample, similar to those of the 70 nm single layer ASI. This variation in the spread in vortex nucleation/annihilation fields is attributed to a tuning of the interlayer coupling between ferromagnetic layers with increased copper thickness, from close coupling with 2 nm Cu to eventually two independent, essentially decoupled ferromagnetic layers. In addition, we note that each of the plots has an open loop around $H=0$, indicative of the presence magnetization from the 30 nm-thick single layer ASI, in contrast to the 70 nm-thick single layer ASI, which showed a linear magnetization change through zero. Figures 2(d) and 2(f) show magnified M–H loops corresponding to the blue highlighted regions in Figs. 2(a)–2(c), where arrows are used to highlight the splitting, shifting, and broadening of reversal features in the 30 nm layer as t_{Cu} is increased. The main reversal features along $\phi = 0^\circ$ are denoted with arrows as A, B, and C. For $t_{Cu} = 2$ nm [Fig. 2(d)], we see two closely spaced reversal features near $H=0$, A and B, peaks which sharpen and split farther apart as the spacer layer thickness increases to $t_{Cu} = 20$ and 40 nm,

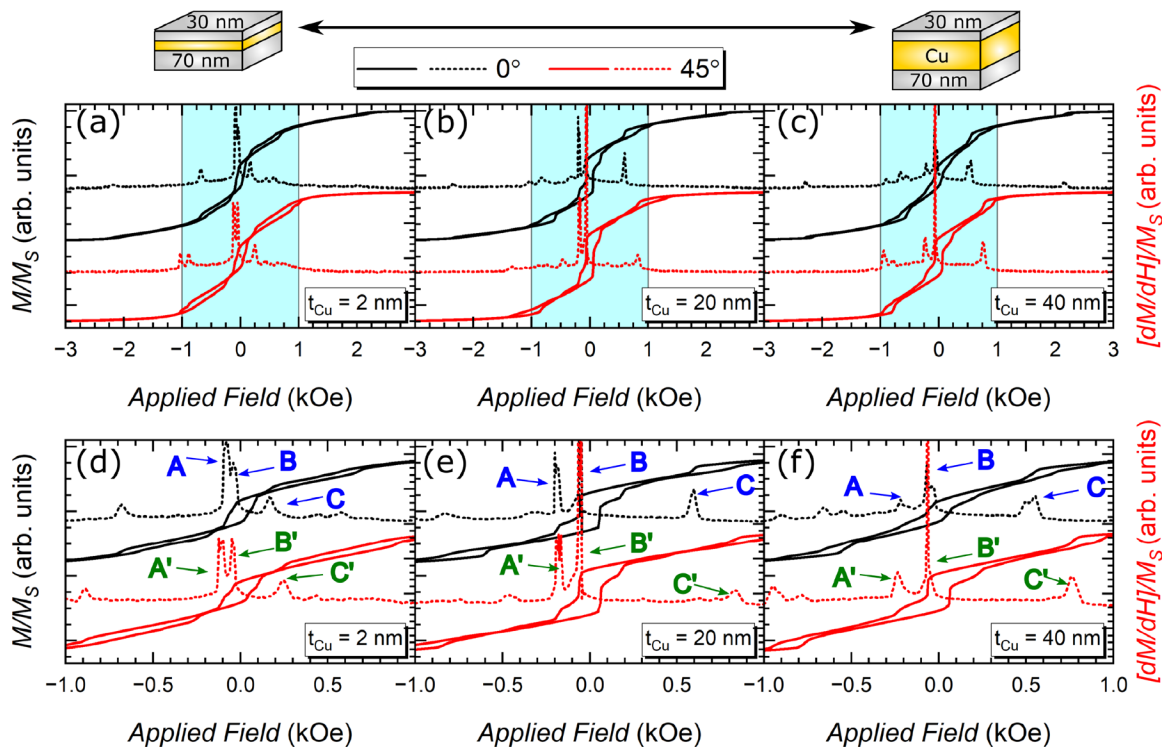


FIG. 2. (a)–(c) Normalized M–H loops, M/M_S , and $(dM/dH)/M_S$ for trilayer arrays with $t_{Cu} = 2, 20,$ and 40 nm, respectively. Highlighted blue region corresponds to the magnified region shown in (d)–(f). Arrows highlight reversal features that are tuned as a function of t_{Cu} . The red and black curves are measured with applied field oriented at 0° and 45° with respect to the square lattice.

from 40 to 120 to 150 Oe. The reversal features associated with C also changes, sharpening and shifting to higher field when $t_{Cu} = 20$ nm, before broadening and moving to a lower field when $t_{Cu} = 40$ nm. Interestingly, the observed shifts are more dramatic along $\phi = 45^\circ$; two features denoted A' and B' are separated by 80 Oe in the $t_{Cu} = 2$ nm case and split further apart with increasing t_{Cu} , while C' has shifted to a much higher field compared to $\phi = 0^\circ$ (near 900 Oe) as t_{Cu} increases. This shows the effect of t_{Cu} is not symmetric along measurement directions in the plane, where tuning interlayer coupling leads to more complex magnetization states.

To understand how the magnetization states evolve with t_{Cu} Fig. 3 shows vector fields plots of the remanent field, H_d , from micro-magnetic simulations, at the midpoint of each ferromagnetic layer, 30 and 70 nm (top and bottom panels, respectively), in the trilayer stack for $t_{Cu} = 5$ and 40 nm (left and center panels, respectively). In Fig. 3(a), we see the formation of complex magnetization states that are neither vortex-like nor macrospin-like in all NMs when $t_{Cu} = 5$ nm, in contrast to $t_{Cu} = 40$ nm [Fig. 3(b)], where near-macrospins and vortices form in the NMs along the easy and hard axes, respectively, much like the 30 nm-thick single layer ASI case. By taking a line-cut of the remanent field along the x axis [Fig. 3(c)] and plotting the x-component (H_{d-x}), we can see how interactions in the 30 nm layer evolves with t_{Cu} . Starting from $t_{Cu} = 0$ nm (red), we see H_{d-x} is strongly modified by the presence of the 70 nm layer (red), but smoothly begins to converge to the 30 nm-thick single layer ASI (black), as t_{Cu} increases to

5 nm (green) and 40 nm (blue). The effect of t_{Cu} on the 70 nm layer is even more dramatic. When $t_{Cu} = 5$ nm [Fig. 3(d)], H_d forms closed loops consistent with a pair of canted vortices in hard-axis NMs and a single vortex in the easy-axis NMs, while at $t_{Cu} = 40$ nm [Fig. 3(e)], H_d is consistent with the formation of single vortex states in all NMs, distinct from the 70 nm single layer ASI. By plotting H_{d-x} [Fig. 3(f)], we see H_{d-x} smoothly diverges from the behavior of the 70 nm-thick single layer ASI as t_{Cu} increases, suggesting that the effect of t_{Cu} is not equivalent between the two ferromagnetic layers in the t_{Cu} range under study. These results confirm that the copper layer offers an additional dimension of control, which allows for an increased number of composite magnetization states at remanence, such as macrospin, single vortex, or bi-vortex states, as well as tunable switching field distribution and nucleation/annihilation fields.

This tunable interlayer coupling leads to striking and controllable changes in the dynamic magnetization behavior. Figures 4(a) shows representative FMR spectra measured with the applied field along $\phi = 0^\circ$ at a frequency of 11.5 GHz. The two dashed lines mark the resonance fields H_{R1} and H_{R2} for the $t_{Cu} = 0$ nm case as a reference. The copper spacer layer causes the resonance modes to shift and broaden, with $t_{Cu} = 2$ nm first lowering H_{R2} to a smaller field, by 0.180 kOe, while keeping H_{R1} essentially unchanged. As t_{Cu} is increased to 20 and 40 nm, both H_{R1} and H_{R2} shift to lower fields, reaching 0.713 and 3.22 kOe. The complex spin dynamics and tunability are further highlighted in measurements along $\phi = 45^\circ$ [Fig. 4(b)], where H'_R

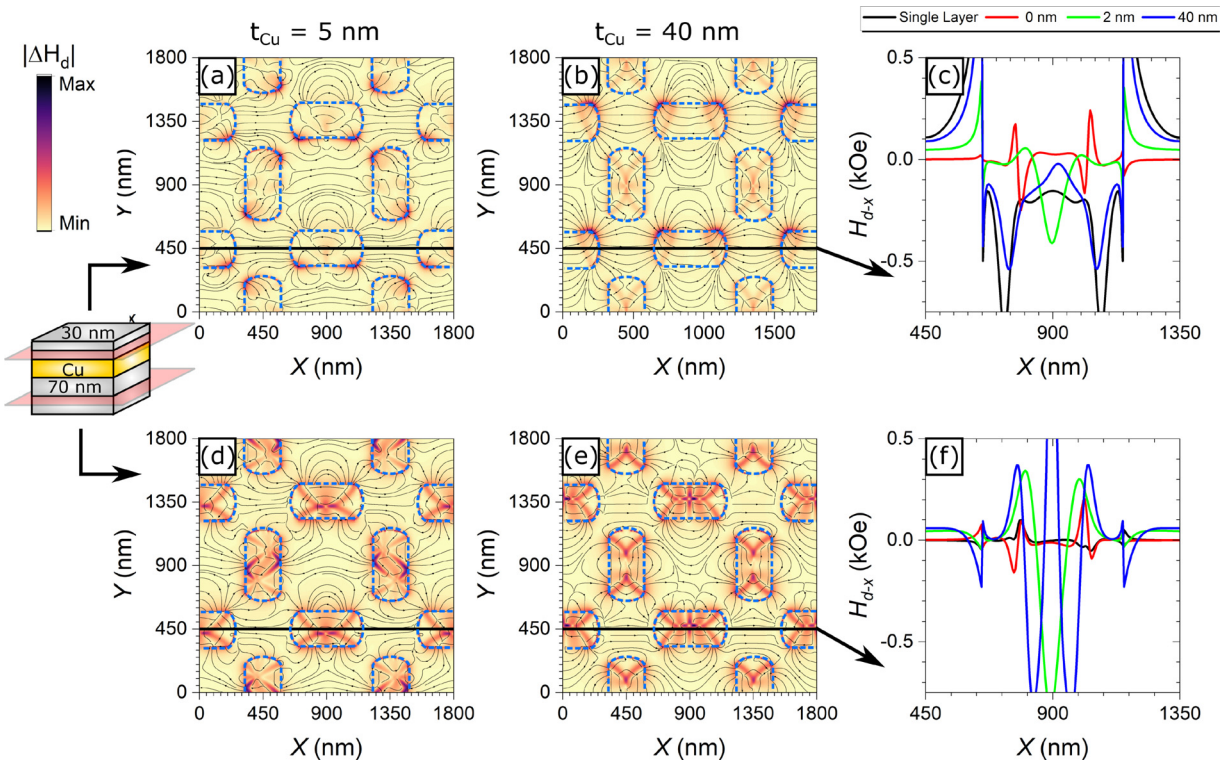


FIG. 3. Simulated remanent field, H_d , at the midpoint of each ferromagnetic layer in the trilayer stack. (a) and (b) H_d at the midpoint of the 30 nm layer for $t_{Cu} = 5$ and 40 nm, respectively. (c) The x-component of H_d (H_{d-x}) in the 30 nm layer along x for several thicknesses of t_{Cu} . (d) and (e) H_d at the midpoint of the 70 nm layer for $t_{Cu} = 5$ and 40 nm, respectively. (f) H_{d-x} along x in the 70 nm layer for several t_{Cu} .

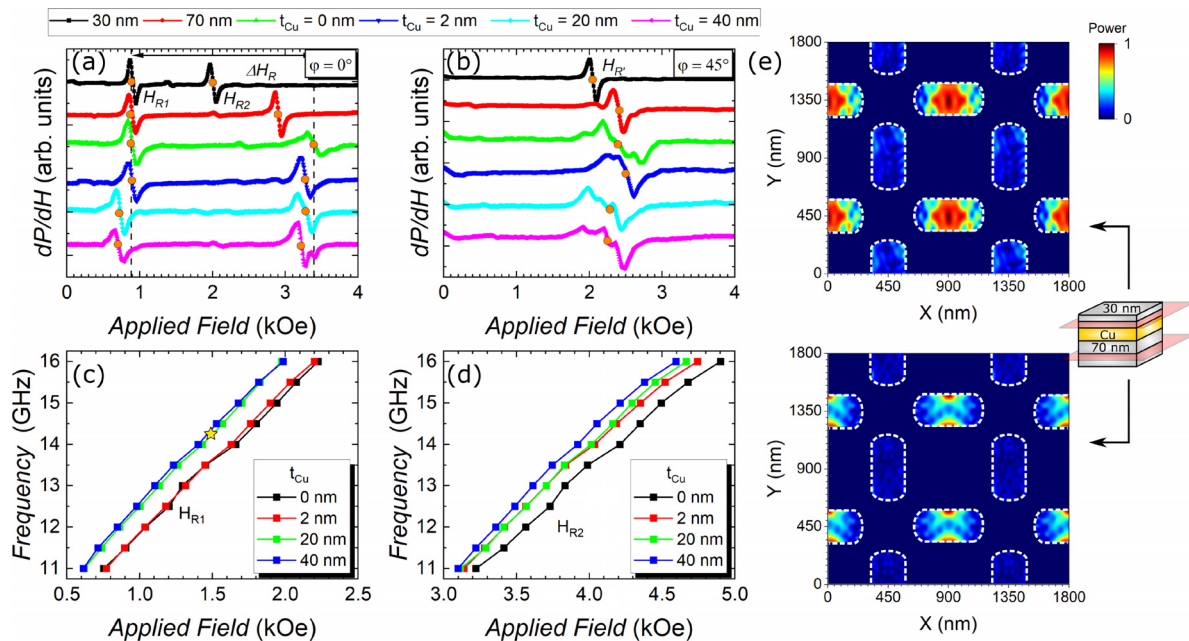


FIG. 4. (a) and (b) Representative FMR spectra at 11.5 GHz for trilayer arrays with increasing t_{Cu} along $\phi = 0^\circ$ and 45° , respectively. (c) and (d) Frequency vs applied field for H_{R1} and H_{R2} measured along $\phi = 0^\circ$ for trilayer arrays with increasing t_{Cu} . (e) Spatial mode profiles along the midpoint of the 30 nm (top) and 70 nm (bottom) layers in a trilayer stack when $t_{Cu} = 40$ nm.

moves to larger fields for $t_{Cu} = 0$ and 2 nm, before a shifting to smaller fields when $t_{Cu} = 20$ and 40 nm. The qualitative behavior of the FMR spectra is also affected by the introduction of the spacer layer with clear, narrow resonance features observed for all samples measured along $\phi = 0^\circ$, while in the 45° case, the resonance features are more complex with the copper layer thickness. Interestingly, the relative spacing between resonance modes (ΔH_R) is also tuned with copper thickness. Figures 4(c) and 4(d) show resonance modes corresponding to H_{R1} and H_{R2} , respectively. The effect on H_{R1} is minimal for $t_{Cu} = 0$ and 2 nm, before shifting dramatically for $t_{Cu} = 20$ and 40 nm, while there is a more gradual shift in H_{R2} as t_{Cu} increases.

This clearly shows an additional degree of tunability accessible via pseudo-3D trilayered structures—the tunability of not only the resonance fields, but also the spacing between the modes. The effect is also clear in the micromagnetic simulations of the spatial resonance modes. Simulated frequency sweeps were done using a sinc pulse of 20 GHz with an amplitude of 50 Oe, with a duration limited to 4 ns in 10 ps time steps. Spatial modes were computed using a Spatial Spectral Analysis Tool,⁵⁵ with an added Hanning window during FFT processing. Figure 4(e) shows the simulated spatial spectra corresponding to an applied field of 1.5 kOe and a resonance peak of 14.07 GHz associated with the fundamental resonance modes of the NMs whose easy axis is aligned with the applied field. The resonance frequency at this field is in good agreement with Fig. 4(c), denoted with a star. The top figure shows the spatial spectra in the 30 nm layer, while the bottom shows that of the 70 nm layer. Here, we see that the spatial mode is heavily localized in the center of the 30 nm layer, while heavily localized at the side walls of the 70 nm layer. This near-complete decoupling of the spatial modes in the two ferromagnetic layers highlights how tuning magnetostatic coupling in trilayer NMs can lead to

complex, layered spatial spin-wave localization and propagation, confirming that spacer-layer thickness variation enables bespoke control of resonance frequencies, spectral spread, and spatial profiles.

In this work, we have examined the static and dynamic behavior of pseudo-3D trilayer structures in square artificial spin ice arrays, where the nanomagnets are two ferromagnetic layers of different thicknesses separated by a nonmagnetic copper layer of varying thickness. Significant tunability of the magnetic properties is observed due to modification of the interlayer coupling between the ferromagnetic layers in the nanomagnets with nonmagnetic layer thickness. We have shown that the interlayer coupling between layers can be used to tune not only the magnetization states and resonance modes, but also the relative spectral spread between them. The experimental results are in good agreement with micromagnetic modeling. Our work shows potential importance as a facile method to move beyond planar structures in the field of reconfigurable magnonic crystals and microwave filter applications.

See the supplementary material for simulated magnetization vs field (M–H) loops of the 30 and 70 nm single layer ASIs, as well as simulated magnetization states at selected fields along the M–H loops.

Dr. Navab Singh is thanked for the DUV templates. The authors thank Dr. David Lloyd and Professor Atsufumi Hirohata for assistance during VSM measurements performed at the University of York. Jay Scott is thanked for SEM imaging of the patterned structures, performed at the GJ Russell Electron Microscopy Facility at Durham University. Micromagnetic simulations were performed using Durham University's NCC cluster. AOA would like to thank the Royal Society Wolfson Fellowship.

AUTHOR DECLARATIONS

Conflict of Interest

The authors have no conflicts to disclose.

Author Contributions

Julius de Rojas: Writing – original draft (equal); Writing – review & editing (equal). **Del Atkinson:** Writing – review & editing (equal). **Adekunle Olusola Adeyeye:** Writing – review & editing (equal).

DATA AVAILABILITY

The data that support the findings of this study are available from the corresponding authors upon reasonable request.

REFERENCES

- ¹I. L. Markov, *Nature* **512**, 147 (2014).
- ²H. Esmaeilzadeh, E. Blem, R. S. Amant, K. Sankaralingam, and D. Burger, in 38th Annual International Symposium on Computer Architecture (ISCA), 2011.
- ³A. Barman, G. Gubbiotti, S. Ladak, A. O. Adeyeye, M. Krawczyk, J. Gräfe, C. Adelman, S. Cotofana, A. Naeemi, V. I. Vasyuchka, B. Hillebrands, S. A. Nikitov, H. Yu, D. Grundler, A. V. Sadovnikov, A. A. Grachev, S. E. Sheshukova, J.-Y. Duquesne, M. Marangolo, G. Csaba, W. Porod, V. E. Demidov, S. Urazhdin, S. O. Demokritov, E. Albisetti, D. Petti, R. Bertacco, H. Schultheiss, V. V. Kruglyak, V. D. Poimanov, S. Sahoo, J. Sinha, H. Yang, M. Münzenberg, T. Moriyama, S. Mizukami, P. Landeros, R. A. Gallardo, G. Carlotti, J.-V. Kim, R. L. Stamps, R. E. Camley, B. Rana, Y. Otani, W. Yu, T. Yu, G. E. W. Bauer, C. Back, G. S. Uhrig, O. V. Dobrovolskiy, B. Budinska, H. Qin, S. van Dijken, A. V. Chumak, A. Khitun, D. E. Nikonov, I. A. Young, B. W. Zingsem, and M. Winklhofer, *J. Phys.: Condens. Matter* **33**, 413001 (2021).
- ⁴A. V. Chumak, V. I. Vasyuchka, A. A. Serga, and B. Hillebrands, *Nat. Phys.* **11**, 453 (2015).
- ⁵A. Hirohata, K. Yamada, Y. Nakatani, I.-L. Prejbeanu, B. Diény, P. Pirro, and B. Hillebrands, *J. Magn. Magn. Mater.* **509**, 166711 (2020).
- ⁶S. Neusser and D. Grundler, *Adv. Mater.* **21**, 2927 (2009).
- ⁷D. Grundler, *Nat. Phys.* **11**, 438 (2015).
- ⁸A. V. Chumak, A. A. Serga, and B. Hillebrands, *Nat. Commun.* **5**, 4700 (2014).
- ⁹A. Haldar and A. O. Adeyeye, *J. Appl. Phys.* **128**, 240902 (2020).
- ¹⁰Q. Wang, A. Hamadeh, R. Verba, V. Lomakin, M. Mohseni, B. Hillebrands, A. V. Chumak, and P. Pirro, *npj Comput. Mater.* **6**, 192 (2020).
- ¹¹Q. Wang, A. V. Chumak, and P. Pirro, *Nat. Commun.* **12**, 2636 (2021).
- ¹²A. Papp, W. Porod, and G. Csaba, *Nat. Commun.* **12**, 6422 (2021).
- ¹³S. Fukami and H. Ohno, *J. Appl. Phys.* **124**, 151904 (2018).
- ¹⁴T. Brächer and P. Pirro, *J. Appl. Phys.* **124**, 152119 (2018).
- ¹⁵J. C. Gartside, K. D. Stenning, A. Vanstone, H. H. Holder, D. M. Arroo, T. Dion, F. Caravelli, H. Kurebayashi, and W. R. Branford, *Nat. Nanotechnol.* **17**, 460 (2022).
- ¹⁶D. A. Allwood, M. O. A. Ellis, D. Griffin, T. J. Hayward, L. Manneschi, M. F. K. Musameh, S. O'Keefe, S. Stepney, C. Swindells, M. A. Trefzer, E. Vasilaki, G. Venkat, I. Vidamour, and C. Wringe, *Appl. Phys. Lett.* **122**, 040501 (2023).
- ¹⁷T. Fischer, M. Kewenig, D. A. Bozhko, A. A. Serga, I. I. Syvorotka, F. Ciubotaru, C. Adelman, B. Hillebrands, and A. V. Chumak, *Appl. Phys. Lett.* **110**, 152401 (2017).
- ¹⁸M. P. Kostylev, A. A. Serga, T. Schneider, B. Leven, and B. Hillebrands, *Appl. Phys. Lett.* **87**, 153501 (2005).
- ¹⁹A. Khitun and K. L. Wang, *J. Appl. Phys.* **110**, 034306 (2011).
- ²⁰T. R. Albrecht, H. Arora, V. Ayanoor-Vitikkate, J.-M. Beaujour, D. Bedau, D. Berman, A. L. Bogdanov, Y.-A. Chapuis, J. Cushen, E. E. Dobisz, G. Doerk, H. Gao, M. Grobis, B. Gurney, W. Hanson, O. Hellwig, T. Hirano, P.-O. Jubert, D. Kercher, J. Lille, Z. Liu, C. M. Mate, Y. Obukhov, K. C. Patel, K. Rubin, R. Ruiz, M. Schabes, L. Wan, D. Weller, T.-W. Wu, and E. Yang, *IEEE Trans. Magn.* **51**, 0800342 (2015).
- ²¹A. Haldar and A. O. Adeyeye, *ACS Nano* **10**, 1690 (2016).
- ²²H. Arava, N. Leo, D. Schildknecht, J. Cui, J. Vijayakumar, P. M. Derlet, A. Kleibert, and L. J. Heyderman, *Phys. Rev. Appl.* **11**, 054086 (2019).
- ²³A. Barman, S. Mondal, S. Sahoo, and A. De, *J. Appl. Phys.* **128**, 170901 (2020).
- ²⁴A. V. Sadovnikov, V. A. Gubanov, S. E. Sheshukova, Y. Sharaevskii, and S. A. Nikitov, *Phys. Rev. Appl.* **9**, 051002 (2018).
- ²⁵A. V. Chumak, A. A. Serga, and B. Hillebrands, *J. Phys. D* **50**, 244001 (2017).
- ²⁶A. V. Chumak, P. Kabos, M. Wu, C. Abert, C. Adelman, A. O. Adeyeye, J. Åkerman, F. G. Aliev, A. Anane, A. Awad, C. H. Back, A. Barman, G. E. W. Bauer, M. Becherer, E. N. Beginin, V. A. S. V. Bittencourt, Y. M. Blanter, P. Bortolotti, I. Boventer, D. A. Bozhko, S. A. Bunyaev, J. J. Carmiggelt, R. R. Cheenikundil, F. Ciubotaru, S. Cotofana, G. Csaba, O. V. Dobrovolskiy, C. Dubs, M. Elyasi, K. G. Fripp, H. Fulara, I. A. Golovchanskiy, C. Gonzalez-Ballester, P. Graczyk, D. Grundler, P. Gruszecki, G. Gubbiotti, K. Guslienko, A. Haldar, S. Hamdioui, R. Hertel, B. Hillebrands, T. Hioki, A. Houshang, C. M. Hu, H. Huebl, M. Huth, E. Iacocca, M. B. Jungfleisch, G. N. Kakazei, A. Khitun, R. Khymyn, T. Kikkawa, M. Kläui, O. Klein, J. W. Klos, S. Knauer, S. Koraltan, M. Kostylev, M. Krawczyk, I. N. Krivorotov, V. V. Kruglyak, D. Lachance-Quirion, S. Ladak, R. Lebrun, Y. Li, M. Lindner, R. Macêdo, S. Mayr, G. A. Melkov, S. Mieszczak, Y. Nakamura, H. T. Nembach, A. A. Nikitin, S. A. Nikitov, V. Novosad, J. A. Otálora, A. Otani, A. Papp, B. Pigeau, P. Pirro, W. Porod, F. Porrati, H. Qin, B. Rana, T. Reimann, F. Riente, O. Romero-Isart, A. Ross, A. V. Sadovnikov, A. R. Safin, E. Saitoh, G. Schmidt, H. Schultheiss, K. Schultheiss, A. A. Serga, S. Sharma, J. M. Shaw, D. Suess, O. Surzhenko, K. Szulc, T. Taniguchi, M. Urbánek, K. Usami, A. B. Ustinov, T. van der Sar, S. van Dijken, V. I. Vasyuchka, R. Verba, S. V. Kusminskiy, Q. Wang, M. Weides, M. Weiler, S. Wintz, S. P. Wolski, and X. Zhang, *IEEE Trans. Magn.* **58**, 0800172 (2022).
- ²⁷S. H. Skjaervå, C. H. Marrows, R. L. Stamps, and L. J. Heyderman, *Nat. Rev. Phys.* **2**, 13 (2019).
- ²⁸S. Gliga, E. Iacocca, and O. G. Heinonen, *APL Mater.* **8**, 040911 (2020).
- ²⁹M. T. Kaffash, S. Lendinez, and M. B. Jungfleisch, *Phys. Lett. A* **402**, 127364 (2021).
- ³⁰A. Talapatra, N. Singh, and A. O. Adeyeye, *Phys. Rev. Appl.* **13**, 014034 (2020).
- ³¹S. Ladak, D. E. Read, G. K. Perkins, L. F. Cohen, and W. R. Branford, *Nat. Phys.* **6**, 359 (2010).
- ³²Y. Lao, F. Caravelli, M. Sheikh, J. Sklenar, D. Gardezabal, J. D. Watts, A. M. Albrecht, A. Scholl, K. Dahmen, C. Nisoli, and P. Schiffer, *Nat. Phys.* **14**, 723 (2018).
- ³³L. Gilbert, Y. Lao, I. Carrasquillo, L. O'Brien, J. D. Watts, M. Manno, C. Leighton, A. Scholl, C. Nisoli, and P. Schiffer, *Nat. Phys.* **12**, 162 (2016).
- ³⁴L. Anginolfi, H. Luetkens, J. Perron, M. G. Flokstra, O. Sendetskiy, A. Suter, T. Prokscha, P. M. Derlet, S. L. Lee, and L. J. Heyderman, *Nat. Commun.* **6**, 8278 (2015).
- ³⁵B. Canals, I.-A. Chioar, V.-D. Nguyen, M. Hehn, D. Lacour, F. Montaigne, A. Locatelli, T. O. Menteş, B. S. Burgos, and N. Rougemaille, *Nat. Commun.* **7**, 11446 (2016).
- ³⁶C. Nisoli, V. Kapaklis, and P. Schiffer, *Nat. Phys.* **13**, 200 (2017).
- ³⁷P. Schiffer and C. Nisoli, *Appl. Phys. Lett.* **118**, 110501 (2021).
- ³⁸M. Wyss, S. Gliga, D. Vasyukov, L. Ceccarelli, G. Romagnoli, J. Cui, A. Kleibert, R. L. Stamps, and M. Poggio, *ACS Nano* **13**, 13910 (2019).
- ³⁹S. Gliga, A. Kákay, R. Hertel, and O. G. Heinonen, *Phys. Rev. Lett.* **110**, 117205 (2013).
- ⁴⁰A. Ghosh, F. Ma, J. Lourembam, X. Jin, R. Maddu, Q. J. Yap, and S. Ter Lim, *Nano Lett.* **20**, 109 (2020).
- ⁴¹V. S. Bhat, S. Watanabe, K. Baumgaertl, A. Kleibert, M. A. W. Schoen, C. A. F. Vaz, and D. Grundler, *Phys. Rev. Lett.* **125**, 117208 (2020).
- ⁴²S. Lendinez and M. B. Jungfleisch, *J. Phys.: Condens. Matter* **32**, 013001 (2019).
- ⁴³A. Haldar, D. Kumar, and A. O. Adeyeye, *Nat. Nanotechnol.* **11**, 437 (2016).
- ⁴⁴S. Saha, J. Zhou, K. Hofhuis, A. Kákay, V. Scagnoli, L. J. Heyderman, and S. Gliga, *Nano Lett.* **21**, 2382 (2021).
- ⁴⁵S. Lendinez, M. T. Kaffash, and M. B. Jungfleisch, *Nano Lett.* **21**, 1921 (2021).
- ⁴⁶S. Sahoo, A. May, A. van Den Berg, A. K. Mondal, S. Ladak, and A. Barman, *Nano Lett.* **21**, 4629 (2021).
- ⁴⁷S. Sahoo, S. Mondal, G. Williams, A. May, S. Ladak, and A. Barman, *Nanoscale* **10**, 9981 (2018).
- ⁴⁸O. V. Dobrovolskiy, N. R. Vovk, A. V. Bondarenko, S. A. Bunyaev, S. Lamb-Camarena, N. Zenbaa, R. Sachser, S. Barth, K. Y. Guslienko, A. V. Chumak, M. Huth, and G. N. Kakazei, *Appl. Phys. Lett.* **118**, 132405 (2021).

- ⁴⁹G. Gubbiotti, X. Zhou, A. O. Adeyeye, G. Varvaro, and M. Kostylev, *Phys. Rev. B* **101**, 224431 (2020).
- ⁵⁰M. Kuchibhotla, A. Talapatra, A. Haldar, and A. O. Adeyeye, *J. Appl. Phys.* **130**, 083906 (2021).
- ⁵¹A. O. Adeyeye and N. Singh, *J. Phys. D* **41**, 153001 (2008).
- ⁵²M. J. Donahue and D. G. Porter, *OOMMF User's Guide Version 1.0* (National Institute of Standards and Technology, Gaithersburg, MD, 1999).
- ⁵³M. Najafi, B. Krüger, S. Bohlens, M. Franchin, H. Fangohr, A. Vanhaverbeke, R. Allenspach, M. Bolte, U. Merkt, D. Pfannkuche, D. P. F. Möller, and G. Meier, *J. Appl. Phys.* **105**, 113914 (2009).
- ⁵⁴W. Wang, C. Mu, B. Zhang, Q. Liu, J. Wang, and D. Xue, *Comput. Mater. Sci.* **49**, 84 (2010).
- ⁵⁵M. Frankowski, J. Chęciński, and M. Czapkiewicz, *Comput. Phys. Commun.* **189**, 207 (2015).